

## Research Article

# Improvement of Photocatalytic Performance for the g-C<sub>3</sub>N<sub>4</sub>/MoS<sub>2</sub> Composite Used for Hypophosphite Oxidation

Wei Guan,<sup>1,2</sup> Kuang He,<sup>1,2</sup> Jianwei Du ,<sup>1,2</sup> Yong Wen,<sup>1,2</sup> Mingshan Li,<sup>1,2</sup> Li Zhuo,<sup>3</sup> Rui Yang,<sup>3</sup> and Kaiming Li<sup>1,2</sup>

<sup>1</sup>South China Institute of Environmental Sciences, Ministry of Ecological Environment, Guangzhou, China

<sup>2</sup>The Key Laboratory of Water and Air Pollution Control of Guangdong Province, South China Institute of Environmental Sciences, MEP, Guangzhou, China

<sup>3</sup>Chongqing Solid Waste Management Center, Chongqing, China

Correspondence should be addressed to Jianwei Du; [dujianwei@scies.org](mailto:dujianwei@scies.org)

Received 24 July 2020; Revised 21 August 2020; Accepted 26 August 2020; Published 15 September 2020

Academic Editor: Changfa Guo

Copyright © 2020 Wei Guan et al. This is an open access article distributed under the Creative Commons Attribution License, which permits unrestricted use, distribution, and reproduction in any medium, provided the original work is properly cited.

The synthesized g-C<sub>3</sub>N<sub>4</sub>/MoS<sub>2</sub> composite was a high-efficiency photocatalytic for hypophosphite oxidation. In this work, a stable and cheap g-C<sub>3</sub>N<sub>4</sub> worked as the chelating agent and combined with the MoS<sub>2</sub> materials. The structures of the fabricated g-C<sub>3</sub>N<sub>4</sub>/MoS<sub>2</sub> photocatalyst were characterized by some methods including X-ray diffraction (XRD), scanning electron microscopy (SEM), and X-ray photoelectron spectra (XPS). Moreover, the photocatalytic performances of various photocatalysts were measured by analyzing the oxidation efficiency of hypophosphite under visible light irradiation and the oxidation efficiency of hypophosphite using the g-C<sub>3</sub>N<sub>4</sub>/MoS<sub>2</sub> photocatalyst which was 93.45%. According to the results, the g-C<sub>3</sub>N<sub>4</sub>/MoS<sub>2</sub> composite showed a promising photocatalytic performance for hypophosphite oxidation. The improved photocatalytic performance for hypophosphite oxidation was due to the effective charge separation analyzed by the photoluminescence (PL) emission spectra. The transient photocurrent response measurement indicated that the g-C<sub>3</sub>N<sub>4</sub>/MoS<sub>2</sub> composites (2.5 μA cm<sup>-2</sup>) were 10 times improved photocurrent intensity and 2 times improved photocurrent intensity comparing with the pure g-C<sub>3</sub>N<sub>4</sub> (0.25 μA cm<sup>-2</sup>) and MoS<sub>2</sub> (1.25 μA cm<sup>-2</sup>), respectively. The photocatalytic mechanism of hypophosphite oxidation was analyzed by adding some scavengers, and the recycle experiments indicated that the g-C<sub>3</sub>N<sub>4</sub>/MoS<sub>2</sub> composite had a good stability.

## 1. Introduction

Sodium hypophosphite is the most common reducing agent during the electroless plating, generating high concentration of hypophosphite wastewater [1, 2]. The main components of plating wastewater are hypophosphite and phosphite, which should be further treatment before discharging into the river or lake avoiding the problem of eutrophication. Due to the high solubility of hypophosphite and phosphite, it is difficult to remove the contaminants by adding Ca<sup>2+</sup> and Fe<sup>3+</sup> ions to generate sediment following by precipitation [3, 4]. Therefore, hypophosphite and phosphite should be oxidized to phosphate, which is easy to recover with the precipitation method. At the same time, the structure of hypophosphite and phosphite is relatively stable, and it is difficult to oxidize

them by ordinary oxidation technology [5], so the technology with strong oxidation ability is needed to solve the problem of hypophosphite oxidation.

Semiconductor photocatalytic technology is a new kind of environmental pollutant reduction technology [6]. The photocatalytic oxidation treatment has the characteristics of easy to handle, no secondary pollution, and a broad potential application [7]. In particular, TiO<sub>2</sub>, as a photocatalytic material, can effectively catalyze the degradation of pollutants in water. It has the advantages of chemical stability, high catalytic activity, good harmlessness to human body, low reaction conditions, and mild selectivity, which has been widely used in the treatment of pollutants that are difficult to be degraded [8]. However, a large band gap (3.2 eV) of TiO<sub>2</sub> indicates that it can only absorb ultraviolet light (only about 3–5% of total

sunlight), which largely inhibits its wide application [9, 10]. So, it is necessary to synthesize a novel photocatalyst that can be responded under visible light irradiation.

Recently, a two-dimensional (2D) conjugated polymer, metal-free graphitic carbon nitride ( $g\text{-C}_3\text{N}_4$ ) has caused much attention due to its suitable band gap of 2.7 eV, which can be responded under visible light irradiation [11, 12]. In addition, the excellent structural stability of  $g\text{-C}_3\text{N}_4$  is widely used in photocatalytic conversion of solar energy and purification of environmental pollutants [13]. Nevertheless, there are some shortcomings for  $g\text{-C}_3\text{N}_4$  as a photocatalyst, such as low utilization rate of light and high recombination rate of photon-generated carrier [14, 15]. Some methods such as structure modification [16], semiconductors coupling [17], elements, and molecular doping [18, 19] were used to modify the  $g\text{-C}_3\text{N}_4$  materials to improve the photocatalytic performance of  $g\text{-C}_3\text{N}_4$ .

Molybdenum disulfide ( $\text{MoS}_2$ ), a 2D metal sulfide material, has the properties of excellent stability and low band gap of 1.2–1.9 eV, which can be easily responded under visible light irradiation and worked as photocatalyst [20, 21]. The valence band electrons can detour into the conduction band under visible light irradiation and leave holes, thus it will generate electron-hole pairs [22]. Due to the small band gap of  $\text{MoS}_2$ , it can be used as a catalyst and cocatalyst, especially doped on some materials, and its photocatalytic performance has been greatly improved [23], which has been widely used in photocatalytic hydrogen evolution and the degradation of organic pollutants [24–26]. The photogenerated electrons of semiconductors could transfer through these noble metals rapidly, and the lifetime of these electrons and holes was prolonged for the noble metal-semiconductor heterostructure materials. Therefore, the prepared  $g\text{-C}_3\text{N}_4/\text{MoS}_2$  composite photocatalyst is beneficial to achieve relatively large specific surface area with abundant active sites for the oxidation reactions.

Herein, a  $g\text{-C}_3\text{N}_4/\text{MoS}_2$  photocatalyst was prepared and shown an improved photocatalytic performance for hypophosphite oxidation under visible light irradiation. The structures of the  $g\text{-C}_3\text{N}_4/\text{MoS}_2$  photocatalyst was analyzed by X-ray diffraction (XRD), scanning electron microscopy (SEM), and X-ray photoelectron spectra (XPS). Moreover, the separation mechanism of generated electron-hole pairs was investigated by photoluminescence (PL) emission spectra, and the photocurrent intensity was analyzed by photoluminescence emission spectra. The reactive species generated during the oxidation process were proved by the quenching experiment. The  $g\text{-C}_3\text{N}_4/\text{MoS}_2$  composite was stable after recycle experiments.

## 2. Experimental

**2.1. Chemicals.** Melamine ( $\text{C}_3\text{H}_6\text{N}_6$ ), absolute methanol ( $\text{CH}_3\text{OH}$ ), sodium molybdate ( $\text{Na}_2\text{MoO}_4 \cdot 2\text{H}_2\text{O}$ ), thioacetamide ( $\text{C}_2\text{H}_5\text{NS}$ ), sodium hypophosphite ( $\text{NaH}_2\text{PO}_2$ ), sodium hydroxide ( $\text{NaOH}$ ), sulfuric acid ( $\text{H}_2\text{SO}_4$ ), sodium sulfate ( $\text{Na}_2\text{SO}_4$ ), and isopropanol ( $(\text{CH}_3)_2\text{CHOH}$ ) were purchased from Sinopharm Chemical Reagent Co., Ltd. (Beijing, China). All the chemical reagents were analytical grade, and

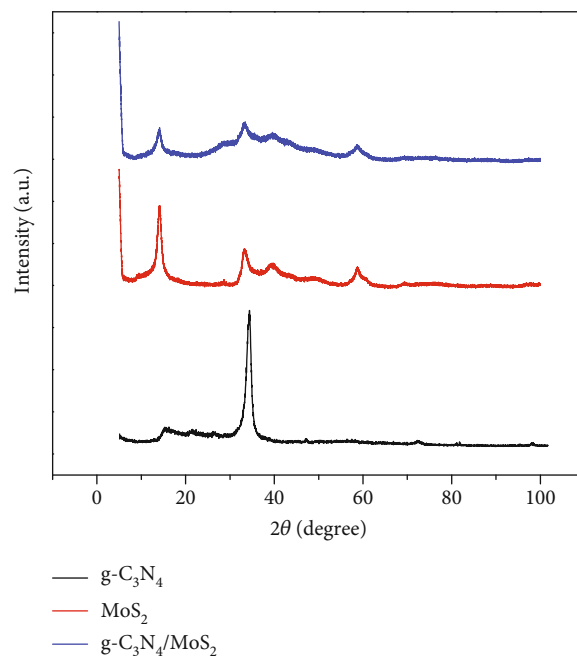


FIGURE 1: XRD patterns of different materials.

the solutions were prepared using Milli-Q water (Millipore, 18.2 M $\Omega$  cm).

**2.2. Preparation of  $g\text{-C}_3\text{N}_4$ .** The  $g\text{-C}_3\text{N}_4$  was prepared as follows: added 5 g melamine into a corundum crucible and then heated at 550°C in a muffle furnace for 2 h to generate a raw  $g\text{-C}_3\text{N}_4$ . Later, the raw  $g\text{-C}_3\text{N}_4$  was dispersed into 50 mL anhydrous methanol and then stirred return for 3 h under 68~70°C. Later, the mixture was dried at 60°C for 12 h under vacuum drying. Finally, cooled down the mixture and grinded with agate mortars, then the yellow  $g\text{-C}_3\text{N}_4$  photocatalyst was synthesized [27].

**2.3. Synthesis of  $g\text{-C}_3\text{N}_4/\text{MoS}_2$  Composite.** The  $g\text{-C}_3\text{N}_4/\text{MoS}_2$  heterojunction was synthesized through the hydrothermal method and shown the following: dissolved 70 mg  $\text{Na}_2\text{MoO}_4 \cdot 2\text{H}_2\text{O}$  and 140 mg  $\text{C}_2\text{H}_5\text{NS}$  into 20 mL deionized water to form a clear solution. Then, added 20 mg  $g\text{-C}_3\text{N}_4$  into the above solution and ultrasound for 45 minutes to generate suspension solution. After that, added 50 ml suspension solution into the teflon reactor and continuously heated at 220°C for 24 h in the drying oven. When the reaction was finished, washed the product with deionized water and anhydrous ethanol for 3 times and centrifugal separation. Finally, the product was heated at 60°C in a vacuum drying oven for 24 h [28].

**2.4. Analysis.** The concentration of hypophosphite was analyzed by ion the chromatography method [29]. The surface morphology of the samples was analyzed by scanning electron microscopy (SEM, Quanta FEG 250). The phase structure of the sample was analyzed by X-ray diffraction (XRD, bruker-d8 Advanc type). The surface properties and chemical states of the sample were analyzed by the X-ray

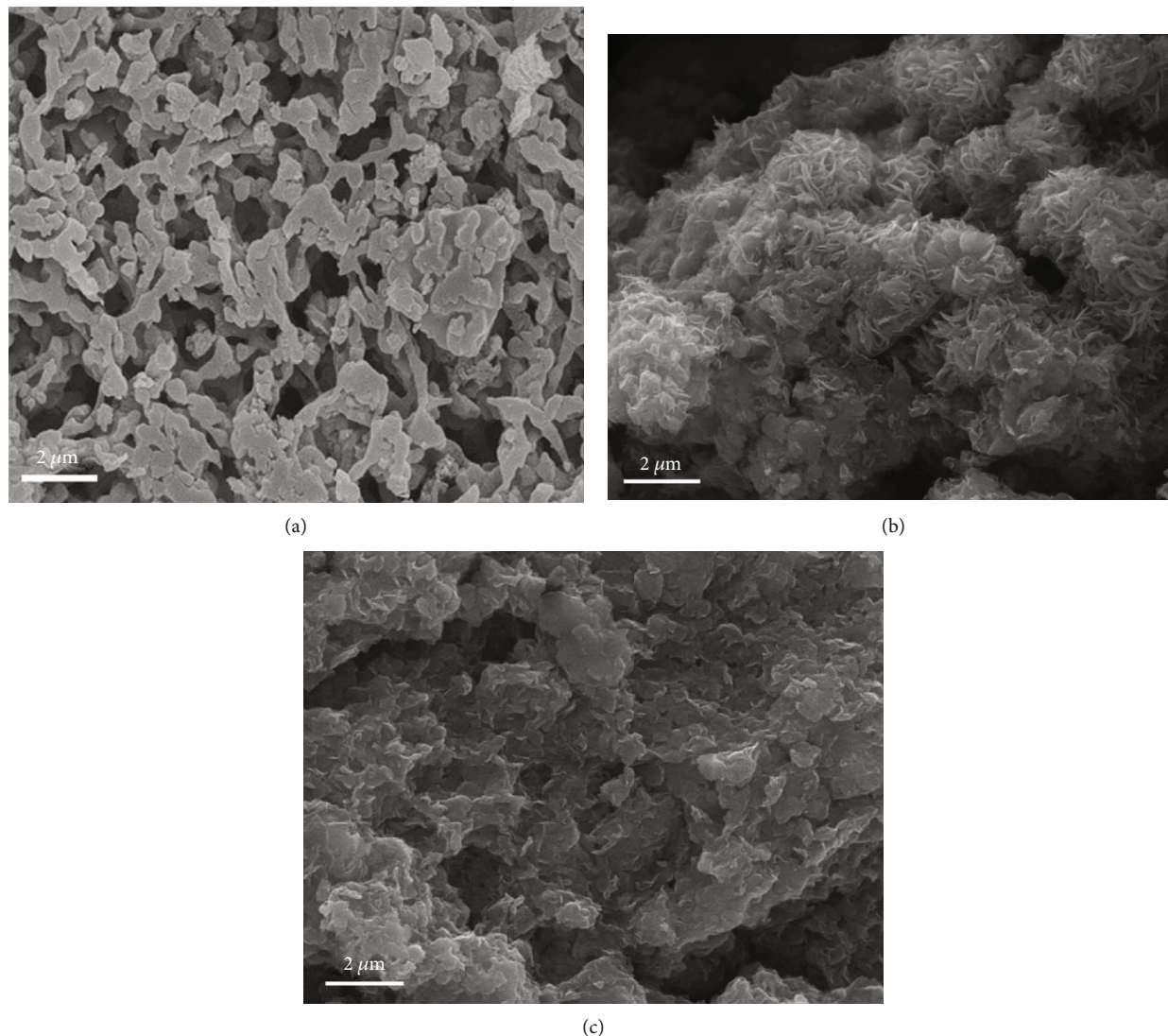


FIGURE 2: SEM analysis of different materials: (a) g-C<sub>3</sub>N<sub>4</sub>, (b) MoS<sub>2</sub>, and (c) g-C<sub>3</sub>N<sub>4</sub>/MoS<sub>2</sub> photocatalyst.

photoelectron spectra (XPS, ULVAC-PHI, INC). The specific surface area and pore size were calculated based on the N<sub>2</sub> physisorption isotherms. At the same time, the photoluminescence spectra were measured with a F-4500 fluorescence (PL) spectrometer, and the photocurrents were measured on a CHI 660B electrochemical system.

**2.5. Analysis of Photocatalytic Performance.** The photocatalytic performance of the generated photocatalyst was evaluated by the oxidation efficiency of hypophosphite under visible light irradiation. During the oxidation process, the light source (35 W) with a 420 nm UV-cutoff filter was placed 12 cm away from the surface of reaction solution. For each photocatalytic experiment, 5 mg photocatalyst was added into the hypophosphite solution (50 ml, 50 mg L<sup>-1</sup>). Before irradiation reaction, the solution was continuously stirred in the dark for 2 h until the adsorption saturation was reached. A small amount of hypophosphite solution was measured every 15 min, and the change of the hypophosphite concentration solution was measured to evaluate the photocatalytic perfor-

mance of the prepared photocatalyst. The oxidation efficiency of hypophosphite was measured as follows:

$$\eta = \frac{C_0 - C_t}{C_0} \times 100\%, \quad (1)$$

where  $C_0$  was the initial concentration of hypophosphite (mg L<sup>-1</sup>);  $C_t$  was the concentration of hypophosphite after irradiation for a certain time  $t$  (min).

### 3. Results and Discussion

**3.1. Analysis of Structure and Morphology for Different Materials.** XRD patterns of the synthesized photocatalyst were analyzed to characterize the crystalline phases and were shown in Figure 1. Two characteristic peaks were observed at 13.2° and 27.6° for pure g-C<sub>3</sub>N<sub>4</sub> photocatalysts. The characteristic peaks observed at 13.2° and 27.6° were indexed as the (110) plane corresponding to the in-plane structure, and the diffraction peak at 27.6° was corresponded to

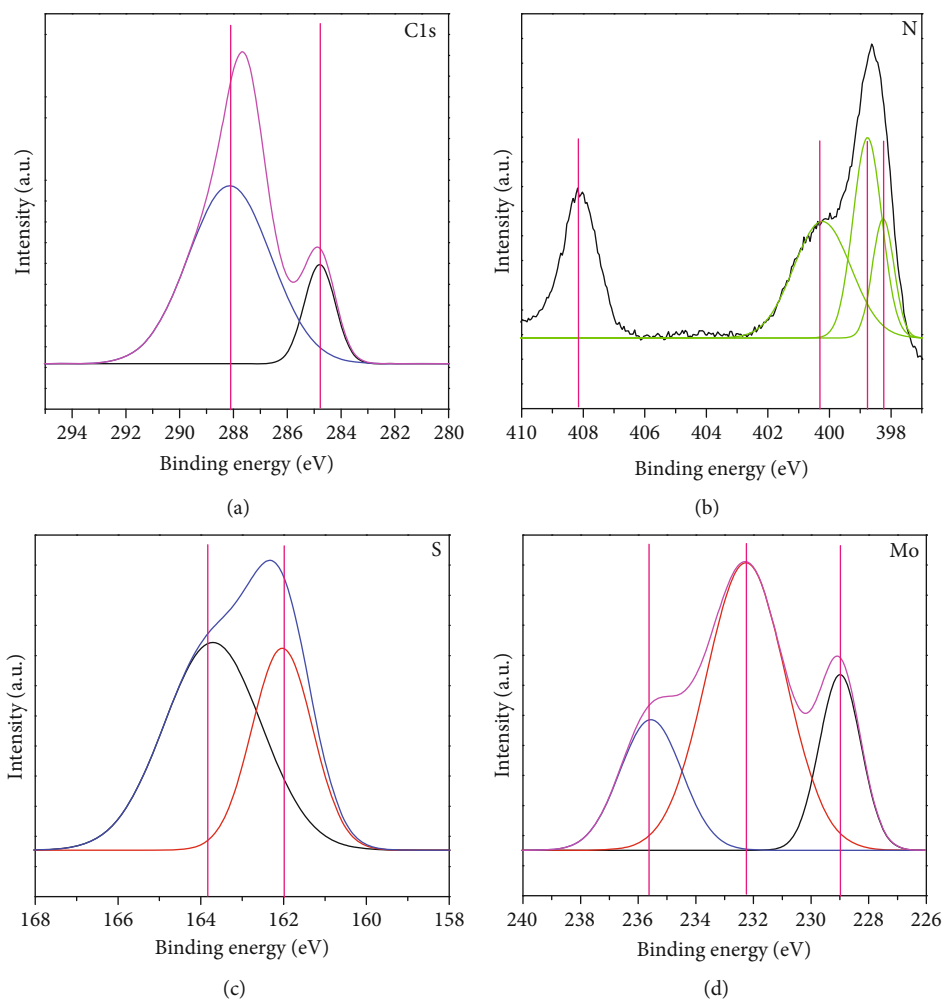


FIGURE 3: XPS spectra of the  $g\text{-C}_3\text{N}_4/\text{MoS}_2$  photocatalyst: (a) C, (b) N, (c) S, and (d) Mo.

interlayer stacking of the conjugated aromatic systems [30]. In addition, two characteristic peaks at  $32.7^\circ$  and  $56.7^\circ$  were observed, which were contributed to the (100) and (110) crystal planes of  $\text{MoS}_2$  (JCPDS No. 37-1492) [31]. According to the results, the formation of  $g\text{-C}_3\text{N}_4/\text{MoS}_2$  photocatalysts was successfully synthesized.

The microstructure of the different materials was shown in Figure 2, layered  $g\text{-C}_3\text{N}_4$  showed many thin nanosheets with a porous structure (Figure 2(a)), and the pure  $\text{MoS}_2$  particles showed a flower-like nanostructure with thin nanosheets avoiding the disordered stacking of  $\text{MoS}_2$  layers (Figure 2(b)). Moreover, the  $g\text{-C}_3\text{N}_4/\text{MoS}_2$  photocatalyst was mainly composed of rhabditiform crystals, and the shape of the synthesized  $g\text{-C}_3\text{N}_4/\text{MoS}_2$  photocatalyst was relatively uniform (Figure 2(c)).

To identify the elements and interaction of as-prepared samples, the XPS spectra of  $g\text{-C}_3\text{N}_4/\text{MoS}_2$  were investigated. As shown in Figure 3(a), the high-resolution XPS spectrum of C 1s exhibited two peaks at 284.8 and 288.2 eV in the  $g\text{-C}_3\text{N}_4/\text{MoS}_2$  photocatalyst assigned to C–C and N=C(–N)<sub>2</sub> of  $g\text{-C}_3\text{N}_4$ , respectively [32]. In the N 1s XPS spectrum (Figure 3(b)), peaks at 398.3, 398.9 and 400.4 eV in the  $g\text{-C}_3\text{N}_4/\text{MoS}_2$  photocatalyst were assigned to C–N, tertiary nitrogen N–C<sub>3</sub>, and C–N–H groups, respectively [33]. The

characteristic peaks of  $2p_{1/2}$  and  $2p_{3/2}$  orbitals for  $\text{S}^{2-}$  were observed at 162.9 and 161.9 eV in the  $g\text{-C}_3\text{N}_4/\text{MoS}_2$  photocatalyst, respectively (Figure 3(c)) [34]. The Mo 3d XPS spectrum of the  $g\text{-C}_3\text{N}_4/\text{MoS}_2$  photocatalyst showed that the two peaks centered at 229.4 and 232.6 eV (Figure 3(d)) assigned to Mo  $3d_{5/2}$  and Mo  $3d_{3/2}$ , respectively, demonstrating that Mo was in the +4 valence state [35].

**3.1.1. Surface Area and Pore Size Distribution.** The nitrogen adsorption-desorption isotherms and pore size distribution of different materials were shown in Figure 4. The specific surface area was calculated to be 114.5, 55.4, and  $147.3 \text{ m}^2 \text{ g}^{-1}$  for  $\text{MoS}_2$ ,  $g\text{-C}_3\text{N}_4$ , and  $g\text{-C}_3\text{N}_4/\text{MoS}_2$  photocatalysts, respectively (Figure 4(a)). Generally, a catalyst with larger surface area could provide many active sites for adsorption and photodegradation towards organic pollutants, resulting in improving the photodecomposition performance. As a result,  $g\text{-C}_3\text{N}_4/\text{MoS}_2$  photocatalysts with higher specific surface area were benefit for improving the photocatalytic oxidation of hypophosphite. Moreover, the pore size distribution of  $g\text{-C}_3\text{N}_4/\text{MoS}_2$  was between 5 and 15 nm, and that of pure  $\text{MoS}_2$  was mainly in the range of 10–25 nm, while no obvious mesopore structure was observed for  $g\text{-C}_3\text{N}_4$  (Figure 4(b)).

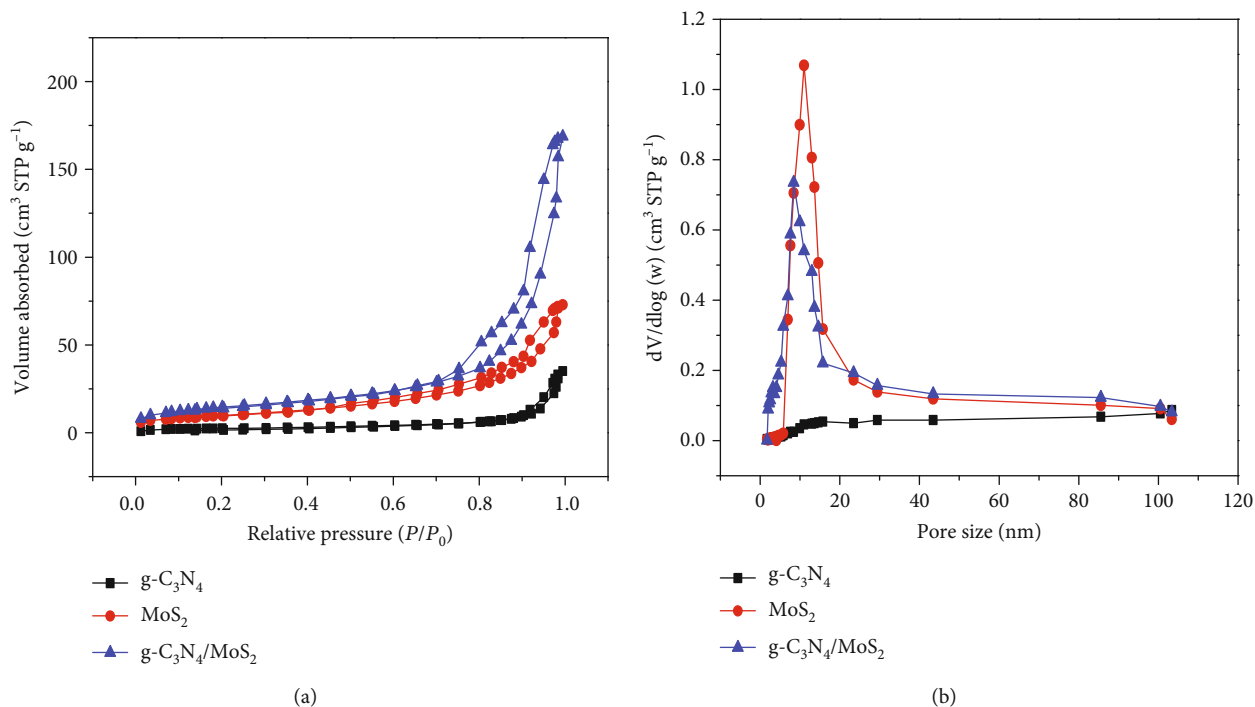


FIGURE 4: (a) Isotherms of nitrogen adsorption and desorption and (b) BJH adsorption pore size distribution of g-C<sub>3</sub>N<sub>4</sub>, MoS<sub>2</sub>, and g-C<sub>3</sub>N<sub>4</sub>/MoS<sub>2</sub>.

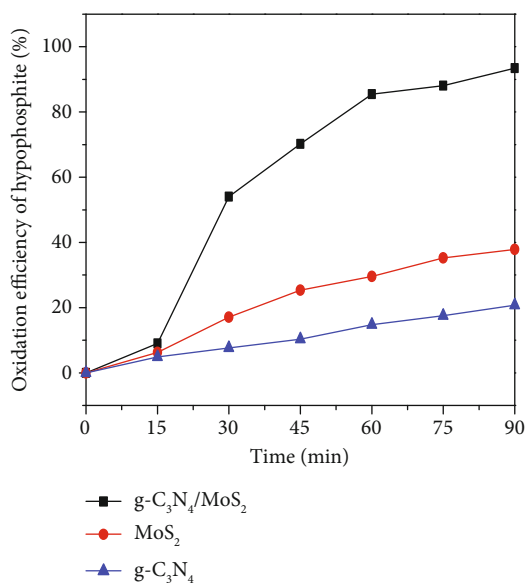


FIGURE 5: The comparison of oxidation efficiency of hypophosphite for different photocatalysts.

**3.2. Analysis of Photocatalytic Activity for Different Photocatalysts.** The oxidation efficiency of hypophosphite for different photocatalysts was shown in Figure 5. The oxidation efficiency of hypophosphite for pure g-C<sub>3</sub>N<sub>4</sub> indicated the lowest photocatalytic performance (20.87%) due to the fast recombination of photo-generated electrons and holes, and the oxidation efficiency of hypophosphite for g-C<sub>3</sub>N<sub>4</sub>/MoS<sub>2</sub> photocatalyst was the highest (93.45%). The photogenerated electrons were transferred from g-

C<sub>3</sub>N<sub>4</sub> to MoS<sub>2</sub>, which could efficiently improve the separate rate of photogenerated electrons and holes. The existence of heterostructure for g-C<sub>3</sub>N<sub>4</sub>/MoS<sub>2</sub> composite limited the recombination of photogenerated electrons and holes. Therefore, the photocatalytic performance of the g-C<sub>3</sub>N<sub>4</sub>/MoS<sub>2</sub> photocatalyst was improved compared with the pure g-C<sub>3</sub>N<sub>4</sub> and MoS<sub>2</sub> photocatalyst.

**3.3. Analysis of Photoluminescence Emission Spectra and Electrochemical Properties.** Enhanced photoactivity performance was ascribed to the fast separation of photogenerated electrons and holes, as confirmed by the photoluminescence technique and transient photocurrent response measurement [36]. According to PL results, the PL spectrum could directly reflect the separation efficiency of photogenerated electron-hole pairs, i.e., the higher intensity of the PL spectrum and the higher recombination rate of photogenerated electron-hole pairs [37, 38]. The PL spectrum of the photocatalyst was shown in Figure 6(a), and all the photocatalysts exhibited a broad emission peak centered at around 460 nm. The PL intensity exhibited the highest value for pure g-C<sub>3</sub>N<sub>4</sub> photocatalyst, while the intensity had become weaker for the g-C<sub>3</sub>N<sub>4</sub>/MoS<sub>2</sub> composite photocatalyst, which was attributed to the improvement of the electron transport induced by quantum confinement effect. Moreover, for the g-C<sub>3</sub>N<sub>4</sub>/MoS<sub>2</sub> photocatalyst, the interaction for g-C<sub>3</sub>N<sub>4</sub> and MoS<sub>2</sub> in the redox potential, it caused the photogenerated electrons transfer from g-C<sub>3</sub>N<sub>4</sub> to MoS<sub>2</sub>, thus reducing the probability of its recombination with holes. In addition, comparing the pure MoS<sub>2</sub>, a distinct red shift was shown, indicating that the g-C<sub>3</sub>N<sub>4</sub>/MoS<sub>2</sub> photocatalysts were more efficient in light harvesting under visible light irradiation.

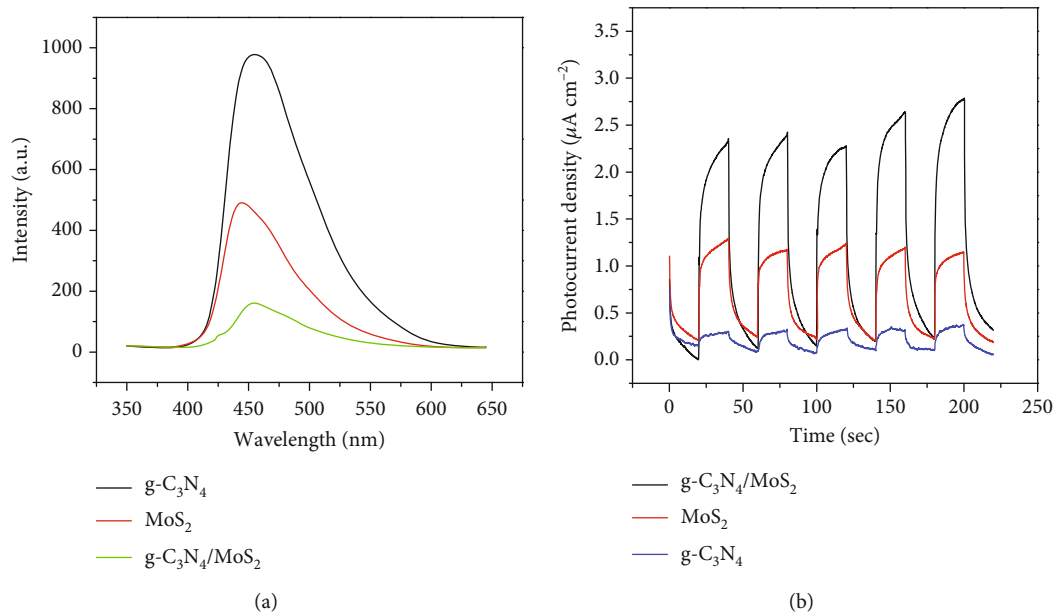


FIGURE 6: The PL spectra and photocurrent density for different photocatalyst.

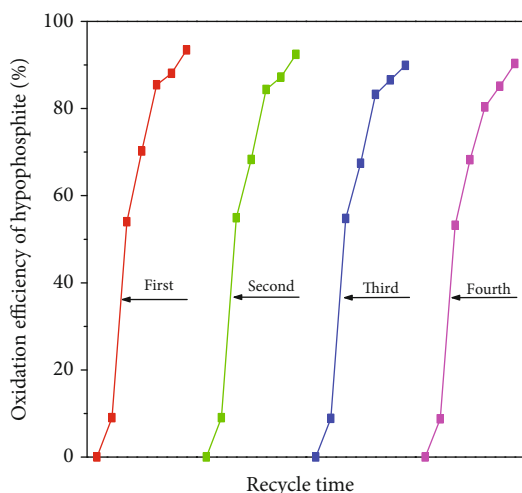


FIGURE 7: The stability analysis of the  $g\text{-C}_3\text{N}_4/\text{MoS}_2$  photocatalyst after recycling experiments.

In addition, the separation of photoinduced carriers of the composites was clarified by the transient photocurrent response measurement [39]. To confirm superior photoinduced carriers in the composites of the  $g\text{-C}_3\text{N}_4/\text{MoS}_2$  photocatalyst, the photocurrent response was evaluated in  $\text{Na}_2\text{SO}_4$  electrolyte [40]. As shown in Figure 6(b), when the  $g\text{-C}_3\text{N}_4/\text{MoS}_2$  electrodes were irradiated under visible light, it showed rapid responsive photocurrents. Moreover, comparing with the pure  $g\text{-C}_3\text{N}_4$  ( $0.25 \mu\text{A cm}^{-2}$ ) and  $\text{MoS}_2$  ( $1.25 \mu\text{A cm}^{-2}$ ), the  $g\text{-C}_3\text{N}_4/\text{MoS}_2$  composites showed 10 times improved photocurrent intensity and 2 times improved photocurrent intensity, respectively. The photocurrent responses were repeatable during on/off cycles under visible light irradiation.

**3.4. Analysis of Stability Performance for the Prepared  $g\text{-C}_3\text{N}_4/\text{MoS}_2$  Photocatalysts.** The stability of the prepared  $g\text{-C}_3\text{N}_4/\text{MoS}_2$  photocatalysts was an important consideration to evaluate the practical applications through four recycling experiments [41]. After each cycle, all the used photocatalysts were collected together, centrifuged, and washed with distilled water, then dried at  $60^\circ\text{C}$  overnight. As shown in Figure 7, the oxidation efficiency of hypophosphite in the recycling experiments was 93.45%, 92.43%, 89.89%, and 90.32%, respectively, which indicated that the structure of photocatalyst was stable during the oxidation of hypophosphite. The results of recycling experiments indicated that the prepared  $g\text{-C}_3\text{N}_4/\text{MoS}_2$  photocatalyst had a strong binding force, which effectively reduced the dissolution of the bulk  $g\text{-C}_3\text{N}_4$  material during the photocatalytic process. Therefore, the  $g\text{-C}_3\text{N}_4/\text{MoS}_2$  photocatalyst had a good stability in the oxidation of hypophosphite.

### 3.5. Photocatalytic Mechanism of Hypophosphite Oxidation.

To analyze the mechanism of photocatalytic oxidation of hypophosphite, the active oxygen species produced under the visible light irradiation were analyzed through the quenching experiment. According to some literature, isopropanol (IPA) worked as the radical quencher for  $\cdot\text{OH}$  radical, while the  $\text{N}_2$  purging was used to reduce the superoxide  $\text{O}_2^{\cdot-}$  radicals [42, 43]. By the ways of adding different scavengers into reaction solutions to remove the corresponding reactive species, the functions of the corresponding reactive species generated in the photocatalytic process was related to the change of the photocatalytic oxidation efficiency of hypophosphite. As shown in Figure 8, the photocatalytic oxidation efficiency of hypophosphite was 93.45% without scavengers. When the IPA was added into reaction solution, and the photocatalytic oxidation efficiency of hypophosphite was decreased to 63%. When  $\text{N}_2$  was blowing into reaction

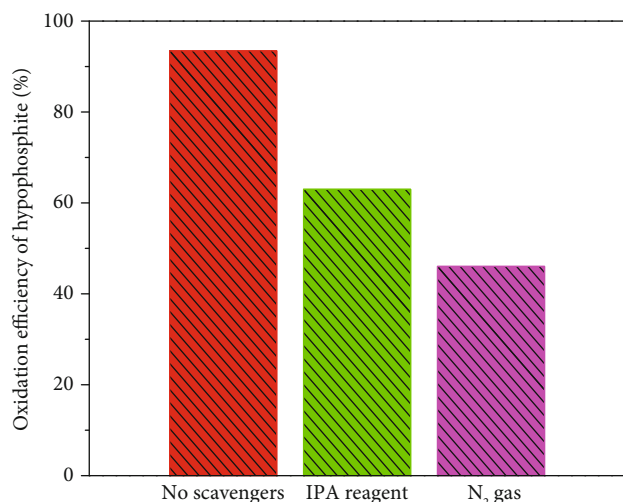


FIGURE 8: Effect of a series of scavengers on the photocatalytic oxidation of hypophosphite.

solution, the photocatalytic oxidation efficiency of hypophosphite was decreased to 46%. According to the results, it was clear that both  $\cdot\text{OH}$  and  $\text{O}_2^{\cdot-}$  radicals were the major reactive species in the photocatalytic reaction system for hypophosphite oxidation. Accordingly, the  $\cdot\text{OH}$  and  $\text{O}_2^{\cdot-}$  radicals had a strong oxidation ability during the photocatalytic oxidation of hypophosphite.

The mechanism of the photocatalytic oxidation of hypophosphite was shown as follows: Firstly, the semiconductor materials ( $\text{g-C}_3\text{N}_4/\text{MoS}_2$ ) absorbed the visible light, and the electron-hole pairs were generated on the surface of photocatalyst. Then, hydroxyl radical was generated through the oxidation of hydroxyl ions ( $\text{OH}^-$ ) with holes. In addition, the superoxide anions were also generated by the molecular reduction of  $\text{O}_2$ , which may attribute to the presence of electrons on the surface of the photocatalyst. The reactive species generated in the photocatalytic system were responsible for hypophosphite oxidation. Furthermore, the photogenerated holes were also responsible for the direct oxidation of the hypophosphite.

#### 4. Conclusion

In the photocatalyst system, the composite  $\text{g-C}_3\text{N}_4/\text{MoS}_2$  indicated higher photocatalytic performance comparing with the pure  $\text{g-C}_3\text{N}_4$  and  $\text{MoS}_2$  photocatalyst. The oxidation efficiency of hypophosphite for the  $\text{g-C}_3\text{N}_4/\text{MoS}_2$  photocatalyst was 93.45%, while the oxidation efficiency of hypophosphite for  $\text{g-C}_3\text{N}_4$  and  $\text{MoS}_2$  were 20.78% and 37.87%, respectively. The mechanism of the improved photocatalytic performance of the  $\text{g-C}_3\text{N}_4/\text{MoS}_2$  photocatalyst for hypophosphite oxidation was analyzed by the photoluminescence technique and transient photocurrent response measurement. The recombination rate of photogenerated electron-hole pairs was reduced, which improved the photocatalytic activity. Moreover, the generated active species were responsible for hypophosphite oxidation analyzed by the quenching experiment.  $\text{OH}$  and  $\text{O}_2^{\cdot-}$  radicals were responsible for the oxidation of hypophosphite. The results of recycling experi-

ments indicated that the  $\text{g-C}_3\text{N}_4/\text{MoS}_2$  photocatalyst had a good stability for hypophosphite oxidation. Therefore, the  $\text{g-C}_3\text{N}_4/\text{MoS}_2$  photocatalyst was an efficient and promising materials for the application of hypophosphite oxidation under visible light irradiation.

#### Data Availability

The data used to support the findings of this study are available from the corresponding author upon request.

#### Conflicts of Interest

There are no conflicts to declare.

#### Acknowledgments

This work was supported by the Ecological Environment Bureau Project of Chongqing (PM-zx555-201911-361); South China Institute of Environmental Sciences, Ministry of Ecological Environment (MEE) Project of Guangzhou (PM-zx703-201904-135); Science and Technology Planning Project of Guangzhou (2017A0103002).

#### References

- [1] A. Stankiewicz, Z. Kefallinou, G. Mordarski, Z. Jagoda, and B. Spencer, "Surface functionalisation by the introduction of self-healing properties into electroless Ni-P coatings," *Electrochimica Acta*, vol. 297, pp. 427–434, 2019.
- [2] S. Li, G. Song, Q. Fu, and C. Pan, "Preparation of Cu-graphene coating via electroless plating for high mechanical property and corrosive resistance," *Journal of Alloys and Compounds*, vol. 777, pp. 877–885, 2019.
- [3] W. Guan, Z. Zhang, S. Tian, and J. Du, "Ti4O7/g-C3N4 for Visible Light Photocatalytic Oxidation of Hypophosphite: Effect of Mass Ratio of Ti4O7/g-C3N4," *Front. Chem*, vol. 6, 2018.
- [4] W. Guan, S. Tian, N. Ma, and X. Zhao, "An electrochemical method through hydroxyl radicals oxidation and deposition of ferric phosphate for hypophosphite recovery," *Journal of Colloid and Interface Science*, vol. 516, pp. 529–536, 2018.
- [5] S. Tian and Z. Zhang, "Photo-electrochemical oxidation of hypophosphite and phosphorous recovery by UV/Fe<sup>2+</sup>/peroxydisulfate with electrochemical process," *Chemical Engineering Journal*, vol. 359, pp. 1075–1085, 2019.
- [6] T. S. Natarajan, K. R. Thampi, and R. J. Tayade, "Visible light driven redox-mediator-free dual semiconductor photocatalytic systems for pollutant degradation and the ambiguity in applying Z-scheme concept," *Applied Catalysis B: Environmental*, vol. 227, pp. 296–311, 2018.
- [7] M. Martin-Somer, C. Pablos, A. de Diego et al., "Novel macroporous 3D photocatalytic foams for simultaneous wastewater disinfection and removal of contaminants of emerging concern," *Chemical Engineering Journal*, vol. 366, pp. 449–459, 2019.
- [8] Y. Ye, H. Bruning, X. Li, D. Yntema, and H. H. M. Rijnaarts, "Significant enhancement of micropollutant photocatalytic degradation using a TiO<sub>2</sub> nanotube array photoanode based photocatalytic fuel cell," *Chemical Engineering Journal*, vol. 354, pp. 553–562, 2018.

- [9] X. Hu, Z. Sun, J. Song, G. Zhang, C. Li, and S. Zheng, "Synthesis of novel ternary heterogeneous BiOCl/TiO<sub>2</sub>/sepiolite composite with enhanced visible-light-induced photocatalytic activity towards tetracycline," *Journal of Colloid and Interface Science*, vol. 533, pp. 238–250, 2019.
- [10] G. Wang, Q. Zhang, Q. Chen et al., "Photocatalytic degradation performance and mechanism of dibutyl phthalate by graphene/TiO<sub>2</sub> nanotube array photoelectrodes," *Chemical Engineering Journal*, vol. 358, pp. 1083–1090, 2019.
- [11] W. Guan and S. Tian, "An effect of crucible volume on the microstructure and Photocatalytic activity of the prepared g-C<sub>3</sub>N<sub>4</sub>," *Journal of Nanoelectronics and Optoelectronics*, vol. 12, no. 8, pp. 781–785, 2017.
- [12] S. Wu, H.-J. Zhao, C.-F. Li et al., "Type II heterojunction in hierarchically porous zinc oxide/graphitic carbon nitride microspheres promoting photocatalytic activity," *Journal of Colloid and Interface Science*, vol. 538, pp. 99–107, 2019.
- [13] G. Zhao, H. Yang, M. Liu, and X. Xu, "Metal-Free Graphitic Carbon Nitride Photocatalyst Goes into Two-Dimensional Time," *Frontiers in Chemistry*, vol. 6, 2018.
- [14] W. Guan, G. Sun, L. Yin, Z. Zhang, and S. Tian, "TiO<sub>2</sub>/g-C<sub>3</sub>N<sub>4</sub> Visible Light Photocatalytic Performance on Hypophosphite Oxidation: Effect of Annealing Temperature," *Frontiers in Chemistry*, vol. 6, 2018.
- [15] W. Kong, X. Zhang, B. Chang et al., "Fabrication of B doped g-C<sub>3</sub>N<sub>4</sub>/TiO<sub>2</sub> heterojunction for efficient photoelectrochemical water oxidation," *Electrochim. Acta*, vol. 282, pp. 767–774, 2018.
- [16] W. Liu, Y. Li, F. Liu, W. Jiang, D. Zhang, and J. Liang, "Visible-light-driven photocatalytic degradation of diclofenac by carbon quantum dots modified porous g-C<sub>3</sub>N<sub>4</sub>: mechanisms, degradation pathway and DFT calculation," *Water Research*, vol. 151, pp. 8–19, 2019.
- [17] J. Dong, Y. Shi, C. Huang, Q. Wu, T. Zeng, and W. Yao, "A new and stable Mo-Mo<sub>2</sub>C modified g-C<sub>3</sub>N<sub>4</sub> photocatalyst for efficient visible light photocatalytic H<sub>2</sub> production," *Applied Catalysis B: Environmental*, vol. 243, pp. 27–35, 2019.
- [18] J. Jing, Z. Chen, and C. Feng, "Dramatically enhanced photoelectrochemical properties and transformed p/n type of g-C<sub>3</sub>N<sub>4</sub> caused by K and I co-doping," *Electrochimica Acta*, vol. 297, pp. 488–496, 2019.
- [19] S. Mao, R. Bao, D. Fang, and J. Yi, "Fabrication of sliver/graphitic carbon nitride photocatalyst with enhanced visible-light photocatalytic efficiency through ultrasonic spray atomization," *Journal of Colloid and Interface Science*, vol. 538, pp. 15–24, 2019.
- [20] Y. Liu, Y. Li, F. Peng et al., "2H- and 1T- mixed phase few-layer MoS<sub>2</sub> as a superior to Pt co-catalyst coated on TiO<sub>2</sub> nanorod arrays for photocatalytic hydrogen evolution," *Applied Catalysis B: Environmental*, vol. 241, pp. 236–245, 2019.
- [21] K. Roy, M. Padmanabhan, S. Goswami, T. P. Sai, S. Kaushal, and A. Ghosh, "Optically active heterostructures of graphene and ultrathin MoS<sub>2</sub>," *Solid State Communications*, vol. 175–176, pp. 35–42, 2013.
- [22] N. Ekthammathat, S. Thongtem, T. Thongtem, and A. Phuruangrat, "Characterization and antibacterial activity of nanostructured ZnO thin films synthesized through a hydrothermal method," *Powder Technology*, vol. 254, pp. 199–205, 2014.
- [23] H. Li, H. Shen, L. Duan et al., "Enhanced photocatalytic activity and synthesis of ZnO nanorods/MoS<sub>2</sub> composites," *Superlattices and Microstructures*, vol. 117, pp. 336–341, 2018.
- [24] O. Yayapao, T. Thongtem, A. Phuruangrat, and S. Thongtem, "Synthesis and characterization of highly efficient Gd doped ZnO photocatalyst irradiated with ultraviolet and visible radiations," *Materials Science in Semiconductor Processing*, vol. 39, pp. 786–792, 2015.
- [25] X. Bai, Y. Du, X. Hu et al., "Synergy removal of Cr (VI) and organic pollutants over RP-MoS<sub>2</sub>/rGO photocatalyst," *Applied Catalysis B: Environmental*, vol. 239, pp. 204–213, 2018.
- [26] J. Akhtar, M. B. Tahir, M. Sagir, and H. S. Bamufleh, "Improved photocatalytic performance of Gd and Nd co-doped ZnO nanorods for the degradation of methylene blue," *Ceramics International*, vol. 46, no. 8, pp. 11955–11961, 2020.
- [27] C. Liang, L. Zhang, H. Guo et al., "Photo-removal of 2,2',4,4'-tetrabromodiphenyl ether in liquid medium by reduced graphene oxide bridged artificial Z-scheme system of Ag@Ag<sub>3</sub>PO<sub>4</sub>/g-C<sub>3</sub>N<sub>4</sub>," *Chemical Engineering Journal*, vol. 361, pp. 373–386, 2019.
- [28] D. Lu, H. Fan, K. K. Kondamareddy et al., "Highly efficient visible-light-induced Photocatalytic production of hydrogen for magnetically retrievable Fe<sub>3</sub>O<sub>4</sub>@SiO<sub>2</sub>@MoS<sub>2</sub>/g-C<sub>3</sub>N<sub>4</sub> Hierarchical microspheres," *ACS Sustainable Chemistry & Engineering*, vol. 6, no. 8, pp. 9903–9911, 2018.
- [29] M. M. McDowell, M. M. Ivey, M. E. Lee et al., "Detection of hypophosphite, phosphite, and orthophosphate in natural geothermal water by ion chromatography," *Journal of Chromatography. A*, vol. 1039, no. 1-2, pp. 105–111, 2004.
- [30] X. Yang, L. Tian, X. Zhao, H. Tang, Q. Liu, and G. Li, "Interfacial optimization of g-C<sub>3</sub>N<sub>4</sub>-based Z-scheme heterojunction toward synergistic enhancement of solar-driven photocatalytic oxygen evolution," *Applied Catalysis B: Environmental*, vol. 244, pp. 240–249, 2019.
- [31] J. Liu, X. Mu, Y. Yang et al., "Construct 3D Pd@MoS<sub>2</sub>-conjugated polypyrrole frameworks Heterojunction with unprecedented photocatalytic activity for Tsuji-Trost reaction under visible light," *Applied Catalysis B: Environmental*, vol. 244, pp. 356–366, 2019.
- [32] X. Shi, M. Fujitsuka, S. Kim, and T. Majima, "Faster Electron injection and more active sites for efficient Photocatalytic H<sub>2</sub> Evolution in g-C<sub>3</sub>N<sub>4</sub>/MoS<sub>2</sub> Hybrid," *Small*, vol. 14, no. 11, pp. 1703277–1703286, 2018.
- [33] V. R. Battula, S. Kumar, D. K. Chauhan, S. Samanta, and K. Kailasam, "A true oxygen-linked heptazine based polymer for efficient hydrogen evolution," *Applied Catalysis B: Environmental*, vol. 244, pp. 313–319, 2019.
- [34] X. Fan, Y. Zhou, G. Zhang, T. Liu, and W. Dong, "In situ photoelectrochemical activation of sulfite by MoS<sub>2</sub> photoanode for enhanced removal of ammonium nitrogen from wastewater," *Applied Catalysis B: Environmental*, vol. 244, pp. 396–406, 2019.
- [35] Y. Dong, C. Huang, and X.-Y. Yang, "Underwater superoleophobic and underoil superhydrophobic surface made by liquid-exfoliated MoS<sub>2</sub> for on-demand oil-water separation," *Chemical Engineering Journal*, vol. 361, pp. 322–328, 2019.
- [36] H. Liu, L. Li, C. Guo, J. Ning, Y. Zhong, and Y. Hu, "Thickness-dependent carrier separation in Bi<sub>2</sub>Fe<sub>4</sub>O<sub>9</sub> nanoplates with enhanced photocatalytic water oxidation," *Chemical Engineering Journal*, vol. 385, p. 123929, 2020.
- [37] L. Li, C. Guo, J. Shen, J. Ning, Y. Zhong, and Y. Hu, "Construction of sugar-gourd-shaped CdS/Co<sub>1-x</sub>S hollow heterostructure as an efficient Z-scheme photocatalyst for hydrogen generation," *Chemical Engineering Journal*, vol. 400, p. 125925, 2020.

- [38] H. Zhang, C. Guo, J. Ren et al., "Beyond  $\text{CoO}_x$ : a versatile amorphous cobalt species as an efficient cocatalyst for visible-light-driven photocatalytic water oxidation," *Chemical Communications*, vol. 55, no. 93, pp. 14050–14053, 2019.
- [39] X. Jin, F. Chen, D. Jia et al., "Influences of synthetic conditions on the photocatalytic performance of ZnS/graphene composites," *Journal of Alloys and Compounds*, vol. 780, pp. 299–305, 2019.
- [40] C. Zhai, M. Sun, L. Zeng et al., "Construction of Pt/graphitic  $\text{C}_3\text{N}_4/\text{MoS}_2$  heterostructures on photo-enhanced electrocatalytic oxidation of small organic molecules," *Applied Catalysis B: Environmental*, vol. 243, pp. 283–293, 2019.
- [41] S. Tian, C. Dang, R. Mao, and X. Zhao, "Enhancement of Photoelectrocatalytic oxidation of cu–cyanide complexes and Cathodic recovery of cu in a metal-free system," *ACS Sustainable Chemistry & Engineering*, vol. 6, no. 8, pp. 10273–10281, 2018.
- [42] N. Seriani, C. Pinilla, and Y. Crespo, "Presence of gap states at Cu/TiO<sub>2</sub>Anatase surfaces: consequences for the Photocatalytic activity," *Journal of Physical Chemistry C*, vol. 119, no. 12, pp. 6696–6702, 2015.
- [43] S. Tian, Y. Li, and X. Zhao, "Cyanide removal with a copper/active carbon fiber cathode via a combined oxidation of a Fenton-like reaction and in situ generated copper oxides at anode," *Electrochimica Acta*, vol. 180, pp. 746–755, 2015.